Novel synthesis of semiconductor chalcohalide anti-perovskites by low-temperature molecular precursor ink deposition methodologies

Ivan Caño^{1,2}, Jonathan W Turnley³, Pol Benítez^{1,2}, Cibrán López Álvarez^{1,2}, José-Miguel Asensi⁴, David Payno⁵, Joaquim Puigdollers^{1,2}, Marcel Placidi^{1,2}, Claudio Cazorla¹, Rakesh Agrawal³, Edgardo Saucedo^{1,2}

Abstract

In recent years, a growing interest in the development of new energy harvesting technologies based on earthabundant, environmentally-friendly semiconductors, has led to the re-discovery of hitherto overlooked materials. Among them, Ag-based chalcohalides stand out for their abundancy and low-toxicity, as well as the crystal structure analogous to perovskite, albeit with cations in place of anions and vice-versa (i.e. anti-perovskite). Until now, inorganic anti-perovskites have generally been studied as solid-state electrolytes. Indeed, Ag₃SI was identified in the 1960s as a superionic conductor. On the other hand, theorical calculations have demonstrated bandgaps in the visible range, suggesting that they could be suitable for PV applications. However, there is little published information on their potential as energy harvesting materials and so far, thin films have been prepared by solid-state reactions or physical vapor deposition techniques at high temperature and/or vacuum conditions. which limits their commercial viability owing to costly, non-scalable processes. In this work, we present a new procedure to synthesize Ag-based chalcohalides by a low-temperature solution-based methodology, using an amine-thiol reactive solvent system to dissolve Ag₂S and AgX (X = Br, I) precursors, followed by spin coating deposition to obtain polycrystalline films. Through this process, it has been possible to synthesize Ag₃S(I_xBr_{1-x}) (x=0-1) films for the first time, which have been characterized, demonstrating the formation of the anti-perovskite phase and a linear correlation between structural parameters and composition. Optical characterization shows bandgap ranging from 0.9 eV (Ag₃SI) to 1.0 eV (Ag₃SBr), with a bowing effect for the intermediate solid solutions. First solar cells prototypes demonstrate photo-response and promising electrical characteristics.

Keywords - Ag₃SI, Ag₃SBr, anti-perovskite structure, chalcohalides, solution processing

Introduction

Metal chalcohalides constitute an extended family of semiconductor materials encompassing different compositions, structural and optoelectronic properties. Since the 1960, several chalcohalide materials have been reported to possess photoconductive, electro-optical and ferroelectric effects, and their wide heterogeneity of compositions and structures lead to a broad bandgap range, potentially suitable for photovoltaics (PV).¹ Nevertheless, these semiconductors have been largely overlooked among the PV community, likely overshadowed by the prevalence of high performance Si in the solar cell market, and the success of other thin film technologies such as CdTe, Cu(In,Ga)Se₂ and lead halide perovskites.^{2,3} Interestingly, recent studies have reported an excellent performance of several chalcohalide materials including SbSI and SbSeI, reaching efficiencies up to a 4% in a very short period of time, benefited by their quasi-1D structure which favors enhanced transport properties.⁴⁻⁷ Likewise, transition metal chalcohalides such as Ag₃SX (X=Br, I) stand out for their crystalline structure analogous to that of the successful halide perovskites, suggesting that they might possess similar defect-tolerant properties. Indeed, their structure presents a perovskite-like arrangement, albeit switching cation sites by anions, and anion sites by cations; thus, the denomination antiperovskite. In fact, very recently, the possible relevance of this type of compounds has been

¹Universitat Politècnica de Catalunya (UPC), EEBE, Av. Eduard Maristany 10-14, Barcelona 08019, Catalonia, Spain

²Universitat Politècnica de Catalunya (UPC), Barcelona Centre for Multiscale Science & Engineering, Av. Eduard Maristany 10-14, Barcelona 08019, Catalonia. Spain

³Purdue Úniversity, Davidson School of Chemical Engineering, Forney Hall of Chemical Engineering, 480 Stadium Mall Drive, West Lafayette, IN 47907-2100

⁴Universitat de Barcelona (UB), Departament de Física Aplicada, Av. Martí i Franquès 1, Barcelona 08028, Spain

⁵Catalonia Institute for Energy Research (IREC), Jardins de les Dones de Negre 1, Sant Adrià del Besòs 08930, Spain

highlighted in several review papers, which also note the lack of methodologies to synthesize suitable thin films for optoelectronic applications.^{1,8}

Ag₃SI and Ag₃SBr were first reported by Reuter and Hardel in 1960,⁹ and after a short time they were identified as superionic conductors by Takahashi and Yamamoto. 10 Consequently, they have been mainly investigated for use as solid electrolytes. However, recent research by Yin, Lapidus et al. have shown that there are at least four polymorphs of Ag₃SI, stable at different temperatures – which diverge upon the ordering of S²-/l⁻ anions and the location of Ag⁺ cations –, of whom only the hightemperature phase can be regarded as superionic with ionic conductivity around 1.5 S/cm (S2-/Idisordered cubic phase). 11 Interestingly, theoretical calculations have shown that Ag anti-perovskites have bandgaps in the 0.9-2.0 eV range, with no consensus for the exact bandgap value, but suggesting that they could be suitable for single-junction solar cells as well as for tandem configuration, thus opening a new horizon of possibilities for this family of materials. 12,13 Despite these promising properties, there is a gap regarding the implementation of anti-perovskites into PV and other energy applications, most likely due to their costly synthesis methodologies. So far, powders and pellets have been essentially fabricated by solid-state synthesis at high temperatures, and ultrathin films have been developed by laser ablation methodologies. 14 These costly and time-consuming synthetic approaches, which involve high temperatures as well as vacuum processing, have hindered the development of this family of materials, resulting in them being largely overlooked as potential semiconductors for energy applications. Remarkably, a revived interest in anti-perovskites has been observed recently, resulting in the first works reporting the synthesis of high-purity Ag₃SBr and Ag₃SI powders at temperatures below 300°C by mechanochemical synthesis. 15 However, to the best of our knowledge, there are no published reports on the synthesis of Ag₃S(Br,I) solid solution compounds in thin film form from low temperature chemical methods, and some of their properties remain unknown in detail, such as the bandgap.

In addition to the ecologically benign nature of their constituents (earth-abundancy, non-toxicity) and suitable bandgaps, Ag_3SX anti-perovskites also stand out for their chemical adaptability. They tolerate different cation and anion-substitutions such as $Ag_3S(Br_xI_{1-x})$ and $(Cu_xAg_{1-x})_3SX$, ¹⁶ which offers a viable approach for bandgap tuning and for adjusting specific properties towards the development of tailored materials for advanced energy applications, including photovoltaics or solid-state batteries.

In this work, Ag₃S(Br_{1-x}I_x) thin films have been prepared using a novel methodology based on the deposition of amine-thiol molecular precursor inks at very low temperatures. With this procedure, polycrystalline anti-perovskite films have been synthesized at temperatures in the 200 – 300°C range, covering the whole Br – I compositional spectrum (x=0 to 1). Composition, structure, morphology and optical properties of the whole family of compounds have been extensively characterized for the first time, demonstrating the formation of the anti-perovskite phase, the impact of anionic substitution to the structural parameters, and a very high compositional uniformity of the films. Also, first simple solar cell prototypes have been manufactured, demonstrating diode behavior and promising optoelectronic properties. Importantly, our method does not require any vacuum or high-temperature treatment at furnace, thus opening up new possibilities for the fabrication and development of anti-perovskites, including their implementation into energy harvesting and power devices. Moreover, solution-based processes are simple, cost-effective and easily scalable, making research and development of these materials for the first time accessible to a larger number of laboratories. Finally, first-principles calculations based on density functional theory (DFT) have been carried out, which are in excellent agreement with the experimental observations after taking into consideration thermal effects (e.g., electron-phonon coupling and ionic diffusion), therefore proving that anti-perovskites are highly anharmonic materials with ostensible ionic conductivity above room temperature.

Materials and methods

Materials. The following materials have been used to fabricate the $Ag_3S(Br_xI_{1-x})$ samples: AgBr (99.998% metal basis) and AgI (99.99% metal basis) were purchased from Thermo-Scientific. Ag_2S (powder, 99.99% metal basis), 1,2-ethanedithiol (EDT; >98%), propylamine (PA; >99%), titanium diisopropoxide bis(acetyl-acetonate) (75% in isopropyl alcohol), poly(3-hexylthiophene-2,5-diyl) (P3HT), thiourea (TU; >99%), and dimethylformamide (DMF) were purchased from Sigma-Aldrich. All chemicals have been used as received.

Solution preparation. Ag₃SX (X = Br, I) molecular precursor inks have been prepared in two steps. First, Ag₂S solutions were prepared by dissolving 0.8 mmols of Ag₂S powder in 790 μ I PA and 410 μ I EDT with continuous stirring at 35°C for 12 to 24 hours (EDT+PA solvent mixture). Similarly, AgX (X = Br, I) solutions were prepared by dissolving 0.2 mmol of AgX powders in 225 μ I PA and 75 μ I EDT with continuous stirring at 35°C. Secondly, when both mixtures were fully dissolved, 250 μ I from the Ag₂S solution were added to the AgX, which was left under stirring at 35°C for 2-4 hours. Importantly, it is recommended to operate with amber or opaque glassware, and perform all the manipulations in darkroom conditions, avoiding exposure to sunlight, to prevent decomposition of AgX into silver metal and Br₂ or I₂. Also, all experiments were performed in an inert atmosphere in a glovebox, using high-purity grade N₂ gas, with O₂ concentration below 0.1 ppm.

Sample preparation. The Ag_3SX amine-thiol precursor inks were deposited by spin-coating onto 2 x 2 cm² FTO-coated soda lime glass substrates, using a SPIN150i-NPP single substrate spin processor by SPS Polos. The deposition was performed in a N_2 glovebox at 2000 rpm for 30 s (1000 rpm acceleration). After each coating, the film was immediately annealed on a preheated hot-plate at temperatures between 200-300°C for 2 min, see **Figure 1** for a schematic layout of the synthesis methodology. The whole process was performed in quasi-dark conditions to avoid the decomposition of precursors into Ag (0). Successive experiments subjected to different synthesis conditions showed that the optimal annealing to obtain pure Ag_3SX samples (free of secondary phases) is at 220°C for 2 min.

Moreover, prototype photovoltaic devices were prepared with a superstrate architecture based on the following structure FTO/TiO $_2$ /Ag $_3$ SX/P3HT/Au, where TiO $_2$ is the electron transport layer and P3HT is the hole transport layer. A 30 nm-thick TiO $_2$ layer was deposited onto the FTO-coated glass substrates by spray-pyrolysis, placing the sample on a hot plate at 500°C, while an atomized diluted TiO $_2$ solution was sprayed by hand sprayer onto it (1 ml titanium diisopropoxide bis[acetylacetonate] solution in 19 ml ethanol). Then, the absorber was synthesized following the process described above. Subsequently, a P3HT solution was prepared dissolving 11 mg P3HT in 1 ml chlorobenzene (1 wt%), which was then deposited onto the absorber by spin-coating (2 steps: 350 rpm for 4 s, 3000 rpm for 20 s), and heated at 170°C for 5 min. Finally, Au was thermally evaporated as the top contact with an active area of 9 mm 2 . The specific devices were prepared with a substrate architecture based on the process described above.

Characterization. Structural characterization by X-ray diffraction (XRD) was performed with a Bruker D8 Advance diffractometer equipped with a Cu X-ray tube (40 kV, 40 mA) and a Sol-X detector with discriminator for the Kβ line and fluorescence effect reduction. The measurements were made using grazing incidence configuration (GIXRD). Absorbance and bandgap measurements were performed by Photothermal Deflection Spectroscopy (PDS) – the setup used here consists of a tungsten halogen lamp, a PTI 01-0002 monochromator, an optical chopper, a position-sensitive detector connected to a lock-in amplifier to measure the deflection of a laser probe beam, and a quartz cuvette filled with Fluorinert liquid (TM FC-40) to place the samples. Scanning Electron Macroscopy (SEM) images were obtained with a Neon40 Crossbeam FIB-SEM workstation from Carl Zeiss, equipped with a GEMINI-SEM column and an INCAPentaFETx3 EDX detector. Preliminary optoelectronic measurements were performed with a Sun 3000 AAA class solar simulator from Abet technologies.

DFT calculations. First-principles calculations based on density functional theory (DFT) were carried out with the PBEsol exchange-correlation energy functional, ^{19,20} as it is implemented in the VASP software. ²¹ The projector-augmented wave method (PAW) was employed to represent the ionic cores by considering the following electronic states as valence: Ag 1s 10d; S 2s 4p; I 2s 5p; Br 2s 5p. ²² The Grimme's et al. D3 scheme was employed for a better treatment of the dispersion interactions in the system. ²³ An energy cutoff of 650 eV and a regular k-point grid center at Gamma of 8x8x8 were used for integration within the Brillouin zone, leading to total energies converging to within 1 meV per formula unit. Atomic relaxations were concluded when the forces in the atoms were all below 0.005 eV/Å. The electronic properties of the different materials were estimated with the accurate screened hybrid exchange-correlation functional HSEsol by considering relativistic spin-orbit coupling effects and adopting the geometries previously determined at the PBEsol+D3 level. ^{24,25} Finite-temperature *ab initio* molecular dynamics simulations were carried out for 2x2x2 and 4x4x4 supercells containing a total of 40 and 320 atoms, respectively. These were performed at T = 200 and 600 K and lasted for 100 and 50 ps, respectively. From all the configurations generated during the dynamical simulations, a total of 10 equally spaced geometries were selected to perform the statistical averages.

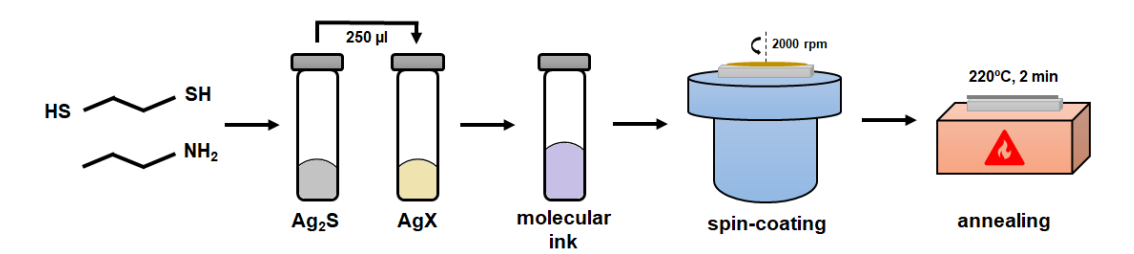


Figure 1: Schematic outlining the synthesis process of Ag₃SX by amine-thiol route, beginning with the preparation of Ag₂S and AgX (X=Br,I) solutions, and the molecular ink. Then, the material is deposited by spin-coating and crystallized by heating treatment on a hot-plate

Results and discussion

The main challenge in the synthesis of Ag-based anti-perovskites by chemical route lies in the difficulty of forming a stable molecular precursor ink, given the poor solubility of silver precursors such as Ag halides and Ag₂S. Interestingly, it has been reported that the solubility of Ag halides increases in polar solvents when 2 TU per halide are present in the solution. ²⁶ However, the mixture of AgX and TU (1:2) in DMF does not lead to successful formation of the anti-perovskite phase. Indeed, structural and compositional characterization revealed that the dominant crystalline phase corresponds to AgBr regardless the annealing conditions, with very small intensity signals compatible, albeit not univocally indexable to Ag₃SBr (see the XRD patterns in Figure S1). This observation is similar to that of Murria et al. where it was revealed that chloride ligands could not be completely displaced by thiolates upon dissolution of CuCl or CuCl₂ in an amine-thiol mixture, resulting in the persistent presence of chlorine in the thin films prepared from these solutions.²⁷ In order to produce an effective molecular precursor ink with the precise stoichiometric amounts of Ag, S and halide, a new approach was devised involving the use of Ag₂S and AgX (X=I, Br) as chemical precursors dissolved in an amine-thiol solvent system. In this case, the very low solubility of Ag₂S constitutes a major limitation when it comes to finding the right solvent. However, it has been shown that amine-thiol mixtures can easily dissolve a wide range of bulk solids which have been generally thought to be insoluble, such as transition metals (i.e., Cu, In, Zn) and chalcogenide compounds, resulting in the designation of the solvent as an alkahest.^{28–32}

A series of anti-perovskite samples have been prepared, which Br-I content ranges from pure bromine up to pure iodine – i.e. $Ag_3S(Br_x|_{1-x})$ with x=1 to x=0 – including three intermediate solid solutions (with x= 0.7, 0.5, 0.3). Structural characterization has been performed by GIXRD, see the patterns in **Figure 2**a. They have been indexed, showing phases corresponding to FTO (the substrate – ICDD file 01-077-0449) and $Ag_3S(Br_x|_{1-x})$, with no apparent secondary phases, suggesting that pure anti-perovskite phases were obtained in all the cases. Interestingly, all the solid solutions containing bromine exhibit

a Pm3m cubic structure (indexed from ICDD file 01-074-0117). Conversely, the pure iodine compound also presents cubic structure, but Im3m symmetry (01-084-1172). As discussed elsewhere, the Aq₃SI system is characterized by having multiple polymorphs which are stabilized at different temperatures. In particular, theoretical analyses have shown that Ag₃SI has two polymorphs with space group Im3m $(\alpha-Ag_3SI)$ and $\alpha^*-Ag_3SI)$, which are characterized by the absence of long-range order of the anion species, i.e. anion sites are randomly occupied by either S²⁻ or I⁻. On the other hand, the cubic Pm3m structure is characterized by the presence of long-range order of the anion species, e.g. S²⁻ and I⁻ occupy vertices and center of the anti-perovskite unit cell respectively, see structures in Figure 2c. Also note that depending on the structure, the three Ag+ per unit cell are randomly distributed over octahedral, tetrahedral or trigonal positions.³³ Significantly, it has been reported that the α phase is stable at higher temperatures (~569 K), with ionic conductivity around 1.5 S/cm, while the α^* phase appears by quenching the α -Ag₃SI polymorph, but has a lower ionic conductivity at 0.13 S/cm. Finally, the Pm3m structure (β-Ag₃SI) is the most stable at room temperature and has the lowest ionic conductivity (approximately two orders of magnitude lower than α*-Ag₃SI). 11,34 Based on its higher stability at room temperature and the lower ionic conductivity, we consider the β-Ag₃S(Br_xI_{1-x}) structure to present the greatest interest for PV applications.

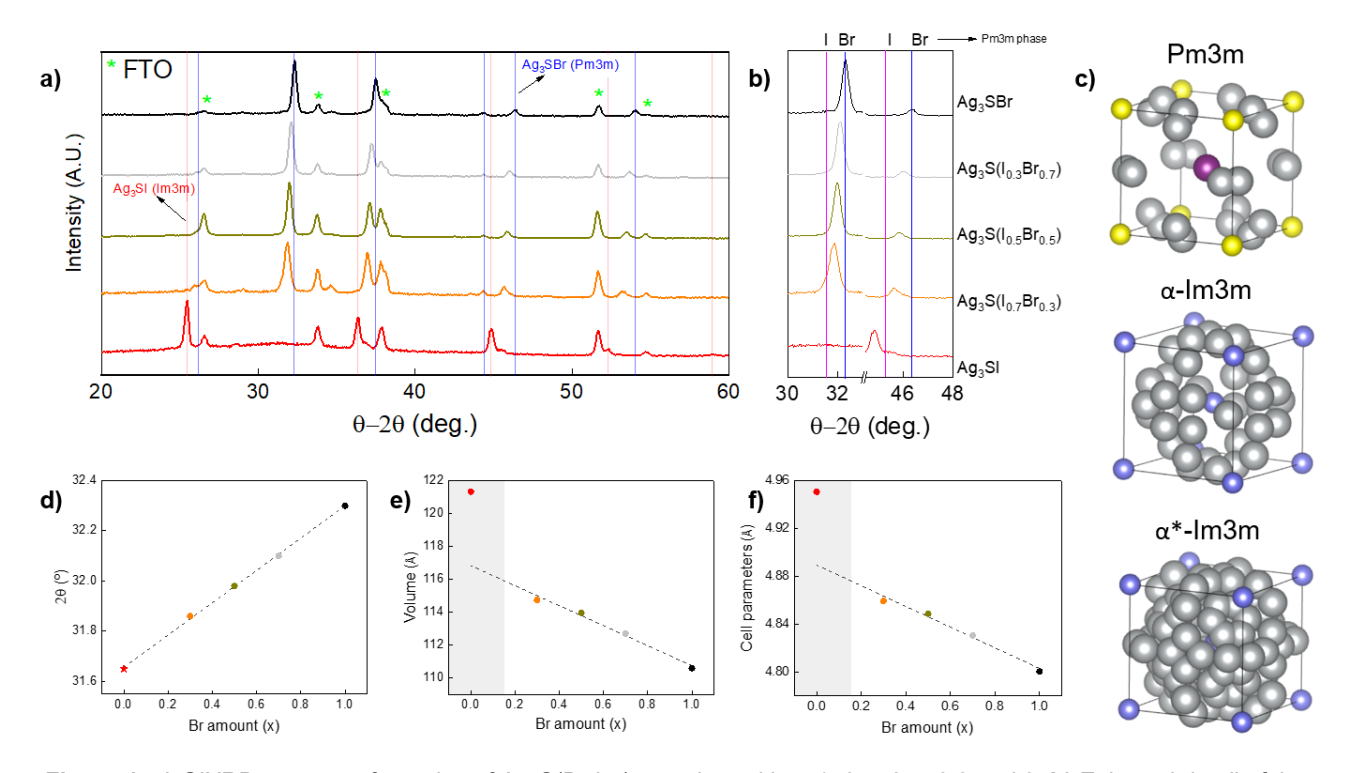


Figure 1: a) GIXRD patterns of a series of Ag₃S(Br_xI_{1-x}) samples, with x=1, 0.7, 0.5, 0.3 and 0. b) Enlarged detail of the patterns in Figure a (blue and pink lines indicate Pm3m Ag₃SBr and Pm3m Ag₃SI, respectively). c) Ag₃SI unit cell structures obtained from *Hull S. et al*,³³ represented with VESTA software: Grey – Ag, Purple – I, Yellow – S, Blue – I/S (anionic disorder)³⁵ d) 2θ position of the diffraction peak that appears around 32° as a function of x. Value for x=0 (star) has been extracted from the Pm3m Ag₃SI ICDD file: 01-084-1167. e) Cell volume as a function of x. f) Lattice parameter as a function of x

Besides these cases of polymorphism, the GIXRD patterns also show that the solid solutions have been successfully formed. Indeed, note that the $Ag_3S(Br_xI_{1-x})$ diffraction peaks shift to lower 2θ values by decreasing x (the Br amount) with respect to the precisely indexed Ag_3SBr Pm3m phase, while the pure iodine structure separates from the trend presenting a completely different pattern (owing to its Im3m symmetry, as discussed above), see **Figure 2**b. A linear correlation is observed between the bromine amount x and the 2θ reflections, which extrapolates consistently to the values for Ag_3SI with

Pm3m cubic symmetry, which has been inserted from tabulated values (01-084-1167 ICDD file). This confirms the existence of a solid solution in the whole Br-I compositional range, and the full miscibility of the Ag₃SBr and Ag₃SI compounds, see **Figure 2**d. Also, analysis and pattern refinement have been performed with FullProf suite,³⁶ applying the Le Bail method for all the crystalline phases observed. As a result, it is demonstrated that the cell volume and lattice parameters increase linearly along with the iodine content, which can be explained by the bigger volume of I⁻ anions with respect Br⁻, resulting in lattice expansion, see **Figures 2**e and f. The linear trend of these figures confirms our hypothesis of the formation of stable Ag₃S(Br_xI_{1-x}) solid solutions with a cubic structure. On the other hand, a structural transition is observed between x=0.3 and x=0 (from Pm3m to Im3m space groups). This transition may be due to the larger size of the I⁻ anion, triggering a phase change under the synthesis conditions used for this work. However, it is necessary to further investigate the formation mechanism of the solid solutions to fully understand the cause of this phenomenon. In addition, the nature of the molecular precursors and their impact on the formation of materials will be studied through solution analysis techniques by mass spectroscopy and nuclear magnetic resonance. See the calculated cell parameters and cell volume in **Table S1**.

To investigate the morphology and composition of the anti-perovskite samples, top-view SEM images have been acquired, along with energy dispersive spectroscopy analysis (EDX) measurements, see Figure 3. At a microscopic level, all the samples present a homogeneous appearance, being constituted by small grains which form a compact layer. Also, the composition is remarkably constant. Notice in the EDX scan mappings that the distributions of Ag, S, and halide are highly uniform in every sample. Likewise, the incorporation of the halide in different proportions is confirmed, as can be noted by the chemical density gradation of the Br / I EDX colour maps as the halide amount (x) changes. Importantly, for the solid solutions, no Br or I-rich areas have been observed, indicating the successful formation of the mixed Ag₃S(Br_xI_{1-x}) compounds instead of segregated phases. Nevertheless, despite the local homogeneity of these films, the 2 x 2 cm² samples are not constituted by an entirely uniform layer, but rather interconnected islands of material, separated by regions where the substrate remains exposed, see Figure S3. This might be caused by a poor adhesion between the coating and the substrate, whereby a different choice of solvents or a different proportion of the solvent mixture could improve the deposition by modifying the surface tension. Alternately, these non-uniformities may result from a nucleation and crystallization process favoring the aggregation of the material, in which case the use of chelating agents or surfactants could offer viable alternatives. All in all, SEM imaging characterization shows remarkably high compositional homogeneity, but it is necessary to improve the uniformity of the layers to achieve continuous samples with a stable thickness.

The absorption spectra of Ag₃S(Br_xI_{1-x}) samples have been acquired by photothermal deflection spectroscopy (PDS), see Figure 4a. With these measurements, the optical absorbance was obtained with a high precision (despite the small thickness and non-uniformity of the layers). 37,38 Then, bandgap was calculated by applying a combined Tauc-Urbach model for the absorption front (see Annex 1 in Supporting Information), resulting in values of 0.88 eV and 0.97 eV for Ag₃SI and Ag₃SBr respectively. These bandgaps are in the appropriate range to absorb most of the solar spectra, making Ag₃SI and Ag₃SBr compatible for single junction solar cells or tandem solar cells as the bottom absorber material. The solid solution samples were also measured, presenting bandgap values around 1.0 eV (see Figure S4). Interestingly, unlike what can be observed with their structural properties, the bandgaps of $Ag_3S(Br_xI_{1-x})$ anti-perovskites do not show a linear trend between the extreme cases (x=1 and x=0). Instead, we observe that the bandgap increases, saturates after a certain value of x (between 0.5 and 0.7), and then decreases again, see Figure 4b. The highest bandgap of this series of samples is 1.029 eV for Ag₃S(Br_{0.5}I_{0.5}). This bandgap nonlinearity, also denominated "bandgap bowing effect", is a common feature of both lead halide and oxide perovskites, which has been attributed to the mismatch between atomic orbitals of the elements that constitute the solid solution.^{39–41} Overall, here it is shown that changing the halide (Br/I) does not have a significant impact on the optical properties, especially the bandgap and absorption coefficient. Hence, we believe that it may be interesting to

explore other areas of the anti-perovskite compositional map, including $(Ag_yCu_{1-y})_3(S_zSe_{1-z})Br$, to discover effective strategies for tuning the bandgap. Lastly, the Urbach tails and large sub-gap absorption indicate the need to optimize the material growth conditions, improving its morphology and crystallinity, and increasing the thickness. Importantly, previous spectroscopic analyses did not show a clear Urbach front, making bandgap measurement extremely difficult, which could only be ascribed as a broad range (0.8 to 2.0 eV for Ag_3SBr). Furthermore, first principle calculations have also yielded a wide dispersion of values, resulting in some uncertainty regarding the optical properties of the antiperovskites, see **Table 1**. ^{15,42} On the other hand, the measurements shown here present a well-defined optical front, and the bandgap values have been obtained through a model that fits correctly with the experimental spectrum. Also, the DFT calculations presented below present good agreement with the measurements, thus advancing towards a better understanding of the properties of this family of materials and the development of a more suitable method for its characterization.

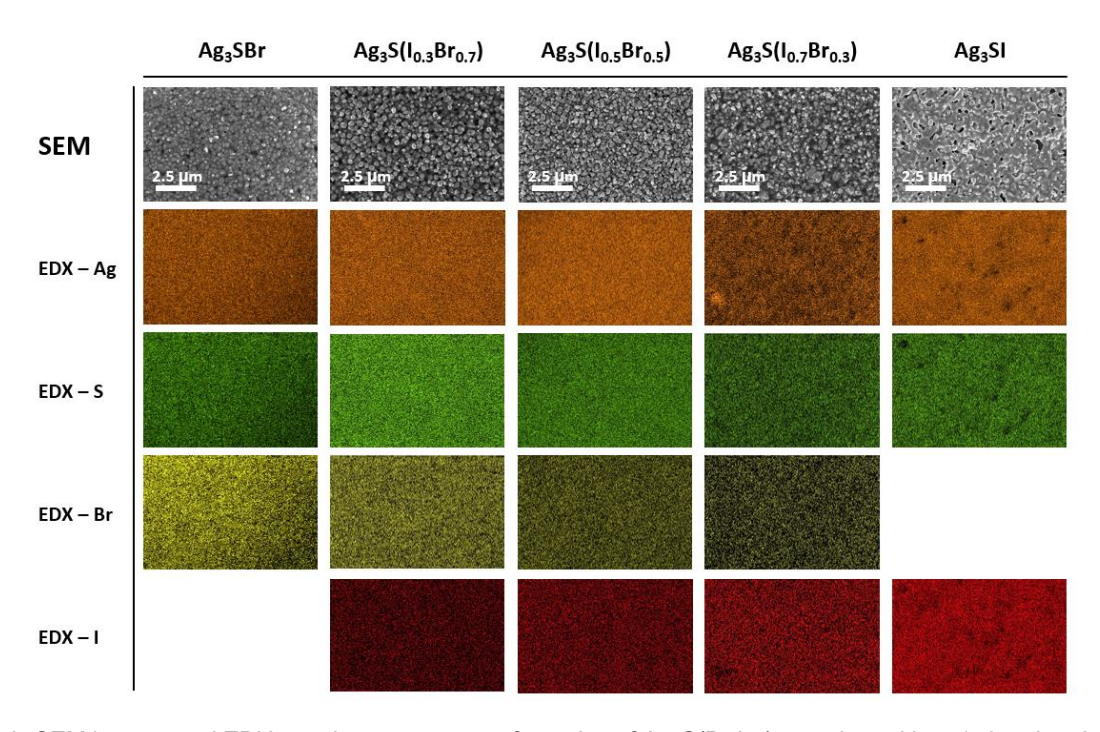


Figure 3: SEM images and EDX top-view scan maps of a series of Ag₃S(Br_xI_{1-x}) samples, with x=1, 0.7, 0.5, 0.3 and 0

Additionally, prototype solar cells have been prepared with the following superstrate architecture: $FTO/TiO_2/Ag_3SX/P3HT/Au$, where TiO_2 works as electron transport layer (ETL) and P3HT is the hole transport layer (HTL). Ag_3SBr and Ag_3SI devices have both shown diode behavior with V_{OC} values up to 150 mV, see **Figures 4** b/c. We highlight that these devices are not optimized, and that the antiperovskite absorber presents a highly irregular, non-uniform morphology, with large and numerous pores which can clearly be responsible for significant shunt losses. Nevertheless, the fact that despite these faults we still obtain a diode current-voltage curve and a photoactive response indicates that these materials have a tangible potential as solar absorbers, and that by improving the uniformity and architecture of the device, their photovoltaic performance can also be enhanced.

The electronic and optical properties of the ternary compounds Ag₃SBr and Ag₃SI have been analyzed using theoretical first-principles methods based on density functional theory (DFT),¹⁹ considering a cubic Pm3m structure for both materials. Accordingly, the lattice parameters and atomic positions were first optimized at the semi-local level,²⁰ and the bandgap and optical absorption coefficients were subsequently estimated using a hybrid exchange-correlation functional, as well as considering spin-

orbit coupling effects. 24,25 For the perfect equilibrium geometries determined at 0 K, bandgaps of 1.93 eV and 1.41 eV were obtained for the Ag₃SBr and Ag₃SI compounds, respectively. Remarkably, these theoretical values present significant discrerpancies with the values measured by PDS in this work (see Figure 4a). Indeed, they are approximately two times larger than the experimental results, indicating a non-satisfactory agreement between empirical evidence and calculations. However, Agbased anti-perovskites have been reported to be extremely anharmonic materials, 43 suggesting that thermal effects such as electron-phonon coupling could play a relevant role to the estimation of the bandgap. In order to consider this possibility, finite-temperature ab initio molecular dynamics simulations at 200 and 600 K were carried out. Then, the bandgap was recalculated by performing statistical averages over a number of uncorrelated configurations obtained at these temperatures. It is worth noting that simulations show the existence of ionic diffusion through mobility of the Ag⁺ cation. Considering these effects, the recalculated bandgap amounted to 1.37 and 1.15 eV for Ag₃SBr (at 200 and 600 K, respectively), and 1.15 and 0.92 eV for Ag₃SI; see **Table 1**, where the bandgap results from this work are presented along with previous calculations and measurements. Overall, after considering these thermal and ionic diffusion effects, the agreement between theoretical and experimental optical properties (bandgap) is excellent within the statistical uncertainties. Importantly, the observation of a wide variation in the DFT-calculated bandgap values between 0 and 600 K (the difference being close to 1 eV), due to the thermal effects, may be one of the reasons why there is so little consensus in the existing literature on the optical properties of chalcohalide anti-perovskites.

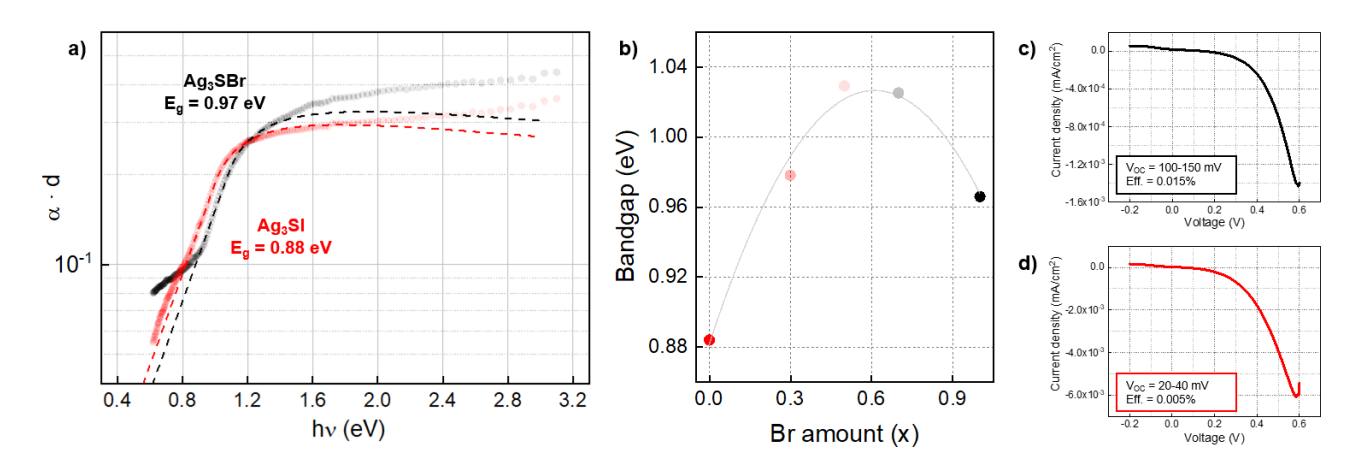


Figure 4: a) Absorption spectra of Ag₃SBr and Ag₃SI films by PDS. **b)** Bandgap as a function of x (Br amount). **c)** Current-voltage characteristics of a Ag₃SBr prototype solar cell. **d)** Current-voltage characteristics of a Ag₃SI prototype solar cell

Table 1: Calculated and measured bandgaps (eV) - * indicates first-principle calculations

	This work				Previous works			
	T=0 K (eV)*	T=200 K (eV)*	T=600 K (eV)*	Measured	Kurita et al.	Palazon et al.	Liu et al.* 12,13	Shimosaka et al.* 13
Ag₃SBr	1.93	1.37 ± 0.07	1.15 ± 0.13	0.97	1.85	0.8 – 1.55	1.95	
Ag₃SI	1.41	1.15 ± 0.10	0.92 ± 0.10	0.88	1.11		1.63	0.88

Finally, the optical properties of both materials have been theoretically studied. **Figure S5** shows the refractive index, extinction coefficient, absorption coefficient, and reflectivity estimated as a function of the incident photon energy. It is appreciated that Ag₃SBr and Ag₃SI materials present similar optical properties, with Ag₃SI exhibiting overall larger values for all the investigated magnitudes. Importantly, from the absorption coefficient plot it can be concluded that both materials possess suitable properties for light harvesting, thus proving that they can be good candidates for photovoltaic applications.

Conclusion

In this work we have demonstrated a solution-based low-temperature methodology to fabricate Ag₃SX (X = Br,I) anti-perovskite materials, based on the deposition of amine-thiol molecular precursor inks. It has been shown that a solvent mixture of ethanedithiol and propylamine allows Ag₃S(Br_xI_{1-x}) layers to be obtained without secondary phases at very low temperature (around 200°C), with a cubic Pm3m structure for the samples containing Br. Likewise, successful synthesis of solid solutions has been demonstrated throughout the whole Br-I range, showing high compositional uniformity and a linearly increasing trend in the lattice parameters as the Br content decreases. The optical bandgap in the 0.9-1.0 eV range and photo-active diode response also indicate that Ag chalcohalide anti-perovskites have a clear potential as semiconductors for energy applications, hence opening the door to a new family of highly versatile earth-abundant materials for thin-film photovoltaics. Finally, DFT calculations shed new light on the controversial anti-perovskite bandgap determination, showing that thermal effects such as electron-phonon coupling and ionic diffusion have a clear impact on the optical properties of the material, which might explain the wide dispersion of results reported so far.

Conflicts of interest

There are no conflicts of interest to declare.

Acknowledgements

This research has received funding from the European Union H2020 Framework Program under through the SENSATE project: Low dimensional semiconductors for optically tunable solar harvesters (grant agreement Number 866018). Other funding from the Ministry of science and innovation of the Government of Spain under the MATER-ONE (PID2020-116719RB-C41) and MIRACLE projects. I.C. acknowledges UPC and Banco Santander for his FPI-UPC PhD scholarship. M.P. acknowledges the financial support from Ministry of science and innovation within the Ramon y Cajal program (RYC-2017-23758). C.C. acknowledges support from the Spanish Ministry of Science, Innovation and Universities under the fellowship RYC2018-024947-I and grant TED2021-130265B-C22. P.B., C.L. and C.C. thankfully acknowledge the computer resources at MareNostrum and the technical support provided by Barcelona Supercomputing Center (RES-FI-1-0006, RES-FI-2022-2-0003, RES-FI-2023-1-0002 and RES-FI-2023-2-0004). E.S. acknowledges the ICREA Academia program. J.W.T. and R.A. are appreciative of the funding support from the National Science Foundation through Grants 1735282-NRT (SFEWS) and 10001536 (INFEWS).

Author contributions

I.C. Conceptualization, formal analysis, investigation, methodology, writing – original draft. J.W.T. Conceptualization, methodology, writing – review & editing. P.B. Data curation, investigation, software, writing – original draft. C.L. Investigation, software, methodology. J.M.A. Formal analysis, methodology. D.P. Methodology. J.P. Funding acquisition, resources, supervision. M.P. Funding acquisition, resources, supervision. R.A. Conceptualization, funding acquisition, methodology, resources, supervision, writing – review & editing. E.S. Conceptualization, funding acquisition, methodology, resources, supervision, writing – review & editing.

References

- (1) Palazon, F. Metal Chalcohalides: Next Generation Photovoltaic Materials? *Solar RRL* **2022**, *6* (2), 2100829. https://doi.org/10.1002/solr.202100829.
- (2) Green, M.; Dunlop, E.; Hohl-Ebinger, J.; Yoshita, M.; Kopidakis, N.; Hao, X. Solar Cell Efficiency Tables (Version 57). *Progress in Photovoltaics: Research and Applications* **2021**, *29* (1), 3–15. https://doi.org/10.1002/pip.3371.
- (3) Zakutayev, A.; Major, J. D.; Hao, X.; Walsh, A.; Tang, J.; Todorov, T. K.; Wong, L. H.; Saucedo, E. Emerging Inorganic Solar Cell Efficiency Tables (Version 2). *JPhys Energy* 2021, 3 (3). https://doi.org/10.1088/2515-7655/abebca.
- (4) Nie, R.; Hu, M.; Risqi, A. M.; Li, Z.; Seok, S. II. Efficient and Stable Antimony Selenoiodide Solar Cells. *Advanced Science* **2021**, *8* (8), 2003172. https://doi.org/10.1002/advs.202003172.
- (5) Nie, R.; Yun, H. S.; Paik, M. J.; Mehta, A.; Park, B. W.; Choi, Y. C.; Seok, S. II. Efficient Solar Cells Based on Light-Harvesting Antimony Sulfoiodide. *Adv Energy Mater* **2018**, *8* (7), 1–7. https://doi.org/10.1002/aenm.201701901.
- (6) Choi, Y. C.; Jung, K. W. One-Step Solution Deposition of Antimony Selenoiodide Films via Precursor Engineering for Lead-Free Solar Cell Applications. *Nanomaterials* **2021**, *11* (12), 3206. https://doi.org/10.3390/nano11123206.
- (7) Jung, K. W.; Choi, Y. C. Compositional Engineering of Antimony Chalcoiodides via a Two-Step Solution Process for Solar Cell Applications. *ACS Appl Energy Mater* **2021**, *5*, 5348–5355. https://doi.org/10.1021/acsaem.1c02676.
- (8) Ghorpade, U. V.; Suryawanshi, M. P.; Green, M. A.; Wu, T.; Hao, X.; Ryan, K. M. Emerging Chalcohalide Materials for Energy Applications. *Chem Rev* **2023**, *123* (1), 327–378. https://doi.org/10.1021/acs.chemrev.2c00422.
- (9) Reuter, B.; Hardel, K. Silbersulfidbromid Und Silbersulfidjodid. *Angew. Chem.* **1960**, 72 (4), 138–139. https://doi.org/10.1002/zaac.19653400308.
- (10) Takahashi, T.; Yamamoto, O. The Ag/Ag3SI/I2 Solid-Electrolyte Cell. *Electrochimia Acta* **1966**, *11*, 779–789. https://doi.org/10.1016/0013-4686(66)87055-X.
- (11) Yin, L.; Murphy, M.; Kim, K.; Hu, L.; Cabana, J.; Siegel, D. J.; Lapidus, S. H. Synthesis of Antiperovskite Solid Electrolytes: Comparing Li3SI, Na3SI, and Ag3SI. *Inorg Chem* **2020**, *59* (16), 11244–11247. https://doi.org/10.1021/acs.inorgchem.0c01705.
- (12) Liu, Z.; Mi, R.; Ji, G.; Liu, Y.; Fu, P.; Hu, S.; Xia, B.; Xiao, Z. Bandgap Engineering and Thermodynamic Stability of Oxyhalide and Chalcohalide Antiperovskites. *Ceram Int* **2021**, *47* (23), 32634–32640. https://doi.org/10.1016/j.ceramint.2021.08.159.
- (13) Shimosaka, W.; Kashida, S.; Kobayashi, M. Electronic Structure of Ag3SI. *Solid State Ion* **2005**, *176* (3–4), 349–355. https://doi.org/10.1016/j.ssi.2004.08.001.
- (14) Tver'yanovich, Y. S.; Bal'makov, M. D.; Tomaev, V. V.; Borisov, E. N.; Volobueva, O. Ion-Conducting Multilayer Films Based on Alternating Nanolayers Ag 3SI, AgI and Ag2S, AgI. *Glass Physics and Chemistry* **2008**, *34* (2), 150–154. https://doi.org/10.1134/S1087659608020065.
- (15) Sebastiá-Luna, P.; Rodkey, N.; Mirza, A. S.; Mertens, S.; Lal, S.; Gaona Carranza, A. M.; Calbo, J.; Righetto, M.; Sessolo, M.; Herz, L. M.; Vandewal, K.; Ortí, E.; Morales-Masis, M.; Bolink, H. J.; Palazon, F. Chalcohalide Antiperovskite Thin Films with Visible Light Absorption and High Charge-Carrier Mobility Processed by Solvent-Free and Low-Temperature Methods. *Chemistry of Materials* **2023**. https://doi.org/10.1021/acs.chemmater.3c01349.
- (16) Beeken, R. B.; Beeken, E. M. Ionic Conductivity in Cu-Substituted Ag3SBr. *Solid State Ion* **2000**, *136*–137, 463–467. https://doi.org/https://doi.org/10.1016/S0167-2738(00)00564-6.

- (17) Salado, M.; Payno, D.; Ahmad, S. Enhancing Operational Stability in Perovskite Solar Cells by Solvent-Free Encapsulation Method. *Sustain Energy Fuels* **2022**, *6* (9), 2264–2275. https://doi.org/10.1039/d1se02054d.
- (18) Juneja, N.; Mandati, S.; Katerski, A.; Spalatu, N.; Daskeviciute-Geguziene, S.; Vembris, A.; Karazhanov, S.; Getautis, V.; Krunks, M.; Oja Acik, I. Sb2S3 Solar Cells with a Cost-Effective and Dopant-Free Fluorene-Based Enamine as a Hole Transport Material. *Sustain Energy Fuels* **2022**, 6 (13), 3220–3229. https://doi.org/10.1039/d2se00356b.
- (19) Cazorla, C.; Boronat, J. Simulation and Understanding of Atomic and Molecular Quantum Crystals. *Rev Mod Phys* **2017**, *89* (3). https://doi.org/10.1103/RevModPhys.89.035003.
- (20) Perdew, J. P.; Ruzsinszky, A.; Csonka, G. I.; Vydrov, O. A.; Scuseria, G. E.; Constantin, L. A.; Zhou, X.; Burke, K. Restoring the Density-Gradient Expansion for Exchange in Solids and Surfaces. *Phys Rev Lett* **2008**, *100* (13). https://doi.org/10.1103/PhysRevLett.100.136406.
- (21) Kresse, G.; Furthmü, J. Efficient Iterative Schemes for Ab Initio Total-Energy Calculations Using a Plane-Wave Basis Set; 1996.
- (22) Blöchl, P. E. Projector Augmented-Wave Method. Phys Rev B 1994, 50 (24), 17953–17979.
- (23) Grimme, S.; Antony, J.; Ehrlich, S.; Krieg, H. A Consistent and Accurate Ab Initio Parametrization of Density Functional Dispersion Correction (DFT-D) for the 94 Elements H-Pu. *Journal of Chemical Physics* **2010**, *132* (15). https://doi.org/10.1063/1.3382344.
- (24) Ganose, A. M.; Cuff, M.; Butler, K. T.; Walsh, A.; Scanlon, D. O. Interplay of Orbital and Relativistic Effects in Bismuth Oxyhalides: BiOF, BiOCl, BiOBr, and BiOl. *Chemistry of Materials* **2016**, *28* (7), 1980–1984. https://doi.org/10.1021/acs.chemmater.6b00349.
- (25) Brothers, E. N.; Izmaylov, A. F.; Normand, J. O.; Barone, V.; Scuseria, G. E. Accurate Solid-State Band Gaps via Screened Hybrid Electronic Structure Calculations. *Journal of Chemical Physics* **2008**, *129* (1). https://doi.org/10.1063/1.2955460.
- (26) Clark, J. A.; Murray, A.; Lee, J. M.; Autrey, T. S.; Collord, A. D.; Hillhouse, H. W. Complexation Chemistry in N,N-Dimethylformamide-Based Molecular Inks for Chalcogenide Semiconductors and Photovoltaic Devices. *J Am Chem Soc* **2019**, *141* (1), 298–308. https://doi.org/10.1021/jacs.8b09966.
- (27) Murria, P.; Miskin, C. K.; Boyne, R.; Cain, L. T.; Yerabolu, R.; Zhang, R.; Wegener, E. C.; Miller, J. T.; Kenttämaa, H. I.; Agrawal, R. Speciation of CuCl and CuCl2 Thiol-Amine Solutions and Characterization of Resulting Films: Implications for Semiconductor Device Fabrication. *Inorg Chem* 2017, 56 (23), 14396–14407. https://doi.org/10.1021/acs.inorgchem.7b01359.
- (28) Koskela, K. M.; Strumolo, M. J.; Brutchey, R. L. Progress of Thiol-Amine 'Alkahest' Solutions for Thin Film Deposition. *Trends in Chemistry*. Cell Press December 1, 2021, pp 1061–1073. https://doi.org/10.1016/j.trechm.2021.09.006.
- (29) Webber, D. H.; Brutchey, R. L. Alkahest for V2VI3 Chalcogenides: Dissolution of Nine Bulk Semiconductors in a Diamine-Dithiol Solvent Mixture. *J Am Chem Soc* **2013**, *135* (42), 15722–15725. https://doi.org/10.1021/ja4084336.
- (30) Turnley, J. W.; Vincent, K. C.; Pradhan, A. A.; Panicker, I.; Swope, R.; Uible, M. C.; Bart, S. C.; Agrawal, R. Solution Deposition for Chalcogenide Perovskites: A Low-Temperature Route to BaMS3Materials (M = Ti, Zr, Hf). *J Am Chem Soc* **2022**, *144* (40), 18234–18239. https://doi.org/10.1021/jacs.2c06985.
- (31) Zhang, R.; Cho, S.; Lim, D. G.; Hu, X.; Stach, E. A.; Handwerker, C. A.; Agrawal, R. Metal-Metal Chalcogenide Molecular Precursors to Binary, Ternary, and Quaternary Metal Chalcogenide Thin Films for Electronic Devices. *Chemical Communications* 2016, 52 (28), 5007–5010. https://doi.org/10.1039/c5cc09915c.

- (32) Guo, J.; Pei, Y.; Zhou, Z.; Zhou, W.; Kou, D.; Wu, S. Solution-Processed Cu2ZnSn(S,Se)4 Thin-Film Solar Cells Using Elemental Cu, Zn, Sn, S, and Se Powders as Source. *Nanoscale Res Lett* **2015**, *10* (1). https://doi.org/10.1186/s11671-015-1045-6.
- (33) Hull, S.; Keen, D. A.; Gardner, J. G.; Hayes, W. The Crystal Structures of Superionic Ag3SI. *J. Phys.: Condens. Matter* **2001**, *13*, 2295–2316. https://doi.org/https://doi.org/10.1088/0953-8984/13/10/321.
- (34) Hoshino, S.; Fujishita, H.; Takashige, M.; Sakuma, T. Phase Transition of Ag3SX (X = I, Br). *Solid State Ion* **1981**, 3 (4), 35–39. https://doi.org/https://doi.org/10.1016/0167-2738(81)90050-3.
- (35) Momma, K.; Izumi, F. VESTA 3 for Three-Dimensional Visualization of Crystal, Volumetric and Morphology Data. *J Appl Crystallogr* **2011**, *44* (6), 1272–1276. https://doi.org/10.1107/S0021889811038970.
- (36) Rodríguez-Carvajal, J.; Roisnel, T.; Gonzales-Platas, J. FullProf Suite. Laboratoire Léon Brillouin, CEA-CNRS, CEN Saclay, France 2005.
- (37) Jackson, W. B.; Amer, N. M.; Boccara, A. C.; Fournier, D. Photothermal Deflection Spectroscopy and Detection. *Appl Opt* **1981**, *20* (8), 1333. https://doi.org/10.1364/ao.20.001333.
- (38) Lopez-Garcia, A. J.; Voz, C.; Asensi, J. M.; Puigdollers, J.; Izquierdo-Roca, V.; Pérez-Rodríguez, A. Ultrathin A-Si:H/Oxide Transparent Solar Cells Exhibiting UV-Blue Selective-Like Absorption. *Solar RRL* **2023**. https://doi.org/10.1002/solr.202200928.
- (39) Goyal, A.; McKechnie, S.; Pashov, D.; Tumas, W.; Schilfgaarde, M. Van; Stevanović, V. Origin of Pronounced Nonlinear Band Gap Behavior in Lead-Tin Hybrid Perovskite Alloys. *Chemistry of Materials* **2018**, *30* (11), 3920–3928. https://doi.org/10.1021/acs.chemmater.8b01695.
- (40) Gao, Q.; Sahin, H.; Kang, J.; Wei, S. H. Origin of Anomalous Band-Gap Bowing in Two-Dimensional Tin-Lead Mixed Perovskite Alloys. *Phys Rev B* **2021**, *104* (6). https://doi.org/10.1103/PhysRevB.104.064204.
- (41) Lee, S.; Levi, R. D.; Qu, W.; Lee, S. C.; Randall, C. A. Band-Gap Nonlinearity in Perovskite Structured Solid Solutions. *J Appl Phys* **2010**, *107* (2). https://doi.org/10.1063/1.3291102.
- (42) Kurita, M.; Nakagawa, K.; Wakamura, K. *Fundamental Absorption Edge of α-Agl-Type Superionic Conductor Ag 3 SBr*; 2000; Vol. 39.
- (43) Wakamura, K.; Miura, F.; Kanashiro, T. Observation of Anomalously Increasing Phonon Damping Constant in the P Phase of the Fast-Ionic Conductor Ag3SI; Vol. 41.
- (44) Kurita, M.; Nakagawa, K.; Akao, F. Photoacoustic Spectrum in Superionic Conductors Ag3SI and AgI. *Jpn J Appl Phys* **1988**, *27* (10), 1920–1922.

Supporting Information

Annex 1: Absorption model used to fit the PDS spectra

The α -d spectra (**Figure 4**a) has been fitted using the following equations of the Urbach-Tauc combined model,

$$for E < E_1 \rightarrow \alpha_{1,Urbach} = \alpha_0 \cdot exp\left(\frac{E}{E_U}\right)$$

$$for \, E > E_1 \to \alpha_{2,Tauc} = \beta \cdot \frac{\sqrt{E - E_g}}{E}$$

where E is the energy ($h\nu$), E_g is the bandgap, E_U is the Urbach energy, α_0 and β are constants of the model, and E_1 is a transition energy near the optical bandgap where the following boundary conditions must be fulfilled.

$$\alpha_{1,Urbach}(E_1) = \alpha_{2,Tauc}(E_1)$$

$$\frac{d\alpha_{1,Urbach}}{dE}(E_1) = \frac{d\alpha_{2,Tauc}}{dE}(E_1)$$

Once the value of E_1 is determined, the system of equations is solved, which determines the value of the direct bandgap (E_a).

Annex 2: Additional figures and tables

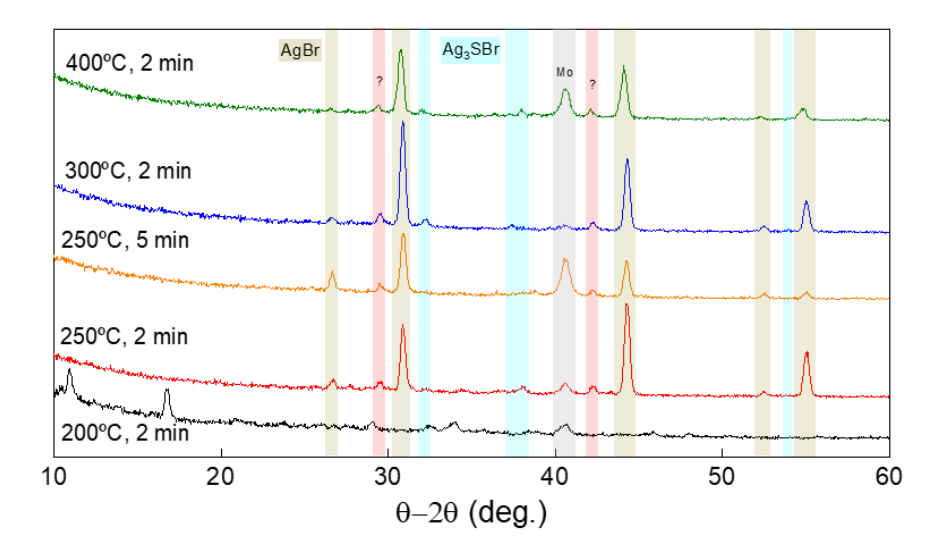


Figure S1: GIXRD patterns of samples prepared with AgBr and TU (1:2) dissolved in DMF. Samples were prepared following this procedure: dissolution of AgBr and TU precursors in DMF to obtain a 0.5 M solution; deposition of solution by drop-casting on Mo-coated glass substrate; drying at 50°C using hot-plate; annealing at temperatures between 200°C-400°C using a hot-plate under N₂ atmosphere

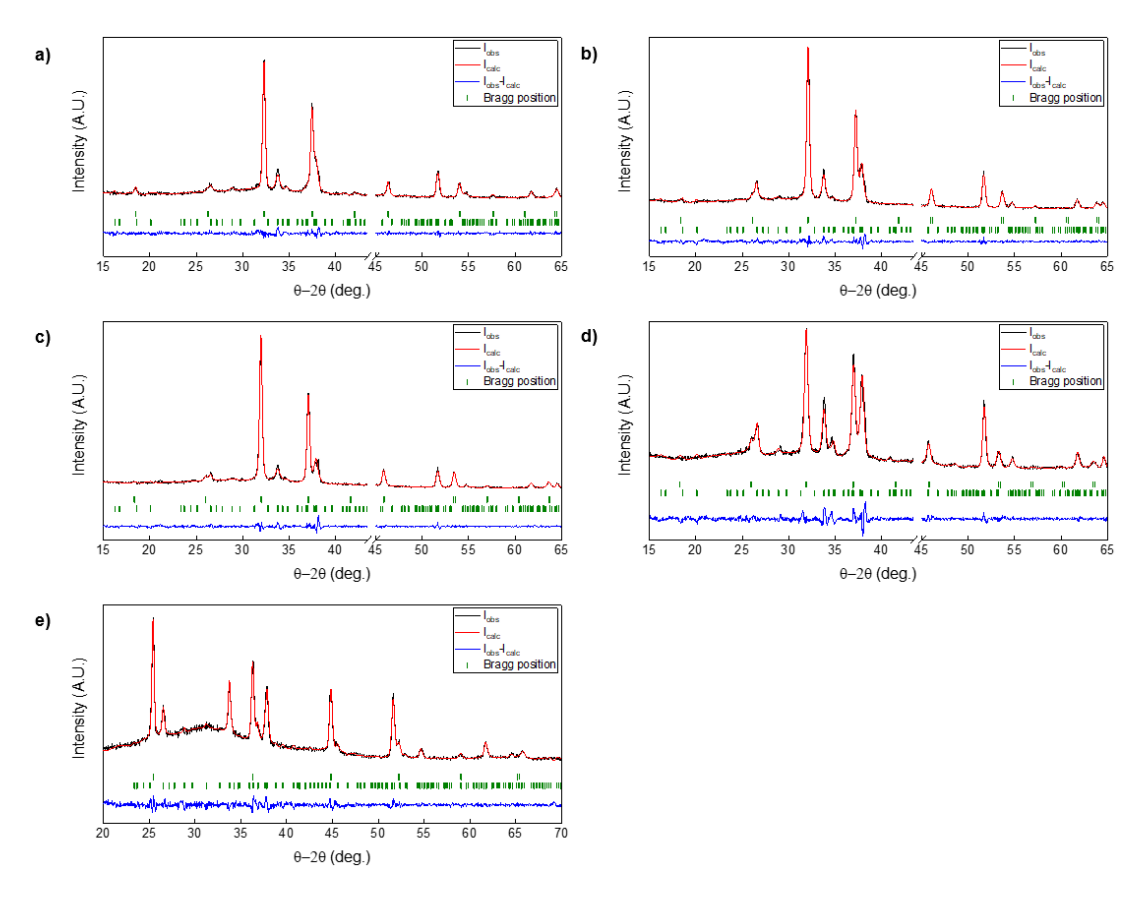


Figure S2: Experimental (red points) and Le Bail (black) refined patterns, along with the difference profile (blue curve) and Bragg reflections (green sticks) of Ag₃S(Br_xI_{1-x}) anti-perovskite samples

Table S1: Cell volume and parameters of Ag₃S(Br_xI_{1-x}) samples. Calculated from Le Bail refinement using the FullProf suite software

х	Vol. (ų)	Cell p. (Å)	Х
1	110.61	4.800	1.43
0.7	112.70	4.830	1.80
0.5	113.97	4.849	1.73
0.3	114.74	4.859	2.03
0	121.42	4.952	1.37

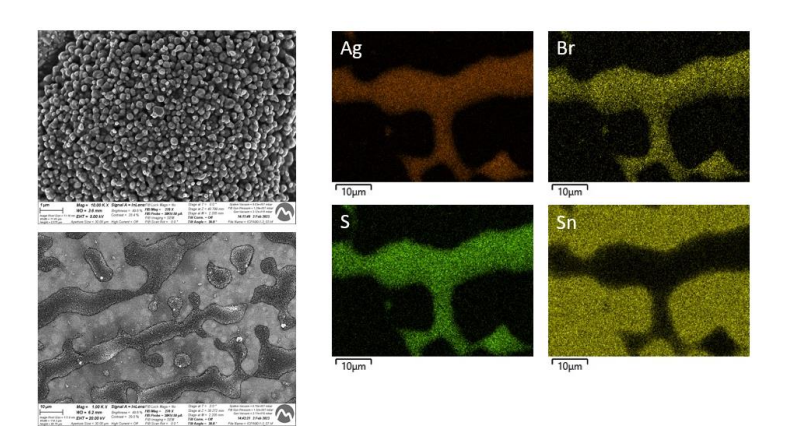


Figure S3: SEM and EDX micrographs of an FTO/Ag₃SBr sample

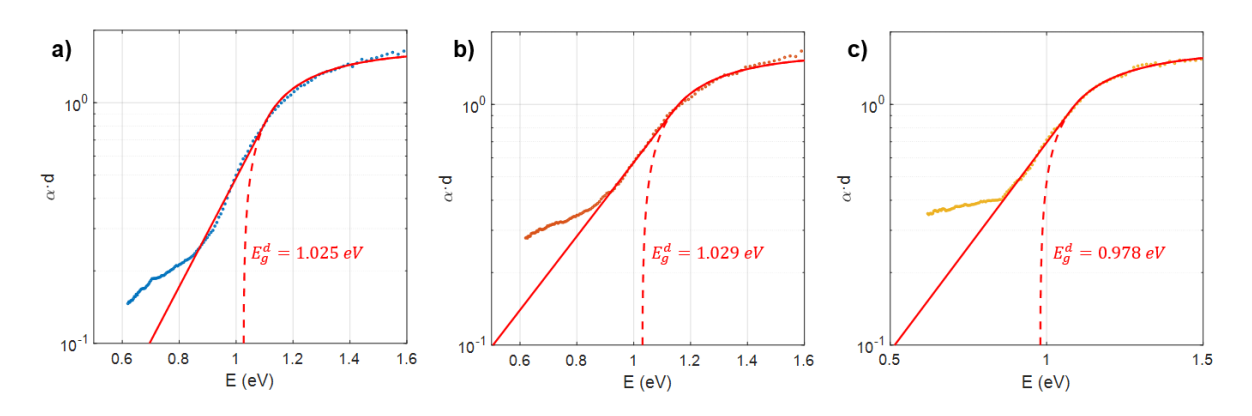


Figure S4: Absorption ($\alpha \cdot d$) spectra of Ag₃S(Br_xI_{1-x}), measured with PDS. a) x=0.7 b) x=0.5 c) x=0.3

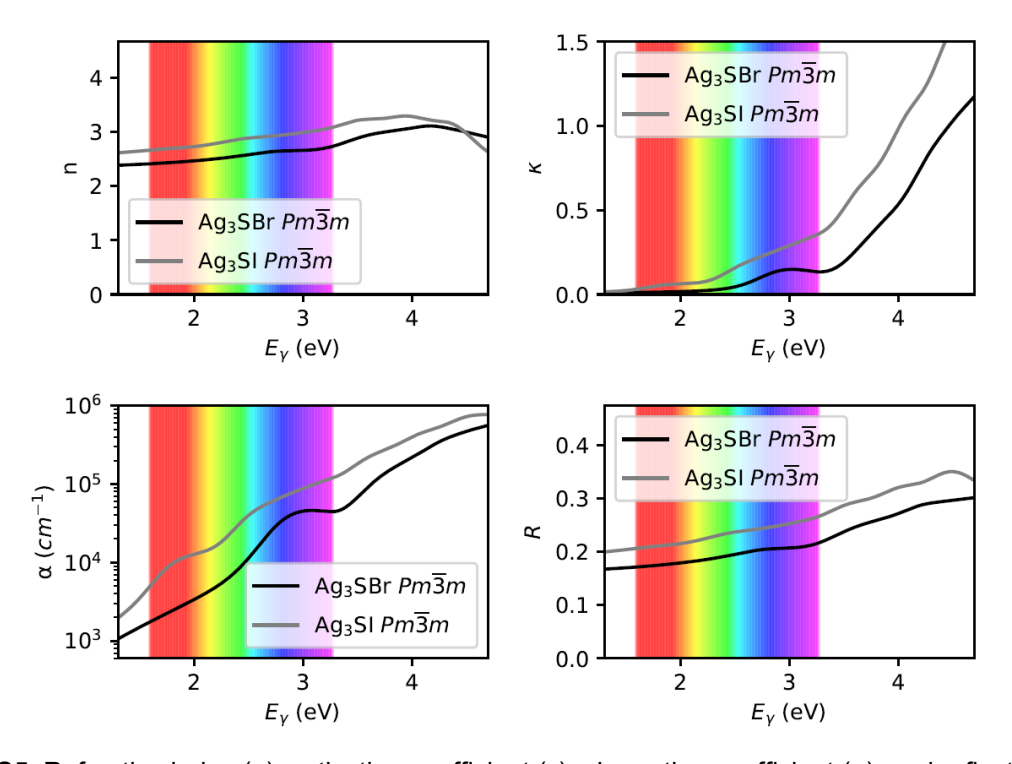


Figure S5: Refractive index (n), extinction coefficient (κ), absorption coefficient (α), and reflectivity (R) estimated as a function of the incident photon energy